Reduced Thermal Resistance of Membrane Fabry-Perot Laser Bonded on Si Through Room-Temperature, Surface-Activated Bonding Assisted by a-Si Nano-Film

Weicheng Fang, Naoki Takahashi, Yoshitaka Ohiso, Tomohiro Amemiya, *Member, IEEE*, and Nobuhiko Nishiyama, *Senior Member, IEEE*

***Abstract*— A membrane distributed-reflector (DR) laser bonded on a Si substrate is a promising light source for on-chip optical interconnection, as it features a low threshold current and enough output power. Benzocyclobutene (BCB) adhesive wafer-bonding or hydrophilic bonding technologies have been used to integrate the membrane laser with Si. However, the thermal conductivity of BCB is low, which results in a high thermal resistance of the membrane laser, and the process of both bonding technologies requires annealing. Thus, the bonded wafer accumulated thermal stress. In this study, we introduce a chemical mechanical polishing (CMP) process to flatten the wafer surface and investigate the surface activated bonding (SAB) based on an Ar fast atom beam (FAB) assisted by an a-Si layer to achieve a room temperature bonding. Based on this room temperature bonding technology, a membrane Fabry-Perot (FP) laser is demonstrated for the first time, and its thermal characteristics are measured. A higher optical saturation current (55 mA) was obtained compared to that of the conventional membrane FP laser (40 mA) with a 2-μm-thick BCB bonding layer. From the lasing wavelength variation against the heat dissipation power and temperature, it was found that a reduction in thermal resistance of approximately 50% (240 K/W to 120 K/W) was achieved by eliminating the BCB layer; the simulation results also showed the same trend.**

***Index Terms*— Surface activated bonding, membrane laser, thermal resistance, chemical mechanical polishing.**

I. Introduction

With the increase in transistor integration density on a chip based on the scaling rule [1], the interconnect between transistors, especially the global wiring, becomes a limiting factor for improving the large-scale integration (LSI) performance because the metallic global wiring suffers from increased resistance and capacitance [2]–[4]. The RC delay affects the bandwidth of data transmission, and the energy dissipation increases because of the Joule heating of the wiring. Recently, a promising solution named "on-chip optical interconnection" [5]–[8] was introduced, and it has received considerable attention with regard to solving this problem. Replacing the electrical interconnection by optical interconnection makes the above-mentioned RC delay and Joule heating negligible. However, to achieve superior overall performance compared with electrical interconnection, compact light sources with ultra-low power consumption are required. In addition, it should be possible to easily integrate the light sources into the Si substrate. Many light sources such as VCSELs [9], [10] and photonic crystal lasers [11], [12] have been developed for achieving on-chip optical interconnections. However, VCSELs require an in-plane light incident mechanism for use as the light source of on-chip optical wiring [13], and photonic crystal lasers require avalanche photodiodes (APDs) for measurement owing to their poor output power [14].

We have proposed a membrane structure-based distributed-reflector (DR) laser on Si bonded by benzocyclobutene (BCB) adhesive bonding at a CMOS-compatible temperature (<300 °C) for on-chip optical interconnection [15]–[17]. A thin semiconductor core layer sandwiched between low-refractive-index materials such as air and SiO_2 is the feature of membrane structure. Therefore, the optical confinement to the thin core layer can be stronger, and optical confinement factor is approximately three times higher than that of conventional semiconductor lasers with semiconductor cladding layers because of this high-index contrast. This stronger optical confinement results in a higher modal gain, resulting in a low-threshold current operation. Thus far, a 0.21 mA low threshold current and 20 Gbit/s high speed operation of short-cavity membrane DR lasers with a low energy cost of 96 fJ/bit has been demonstrated [18].

Although high speed and low energy cost operations have been demonstrated, issues with the temperature characteristics are yet to be addressed. For high-temperature operation, Bragg

Manuscript received October 6, 2021; revised December 13, 2021; accepted January 13, 2022. Date of publication January 25, 2022; date of current version February 4, 2022. This work was supported in part by the JSPS KAKENHI under Grant 21J14548, Grant 20H02200, and Grant 19H02193; and in part by the JST-CREST under Grant JPMJCR15N6. *(Corresponding author: Weicheng Fang.)*

Weicheng Fang, Naoki Takahashi, and Yoshitaka Ohiso are with the Department of Electrical and Electronic Engineering, Tokyo Institute of Technology, Tokyo 152-8552, Japan (e-mail: fang.w.aa@m.titech.ac.jp; takahashi.n.av@m.titech.ac.jp; oiso.yoshitaka@ee.e.titech.ac.jp).

Tomohiro Amemiya and Nobuhiko Nishiyama are with the Department of Electrical and Electronic Engineering, Institute of Innovative Research, Tokyo Institute of Technology, Tokyo 152-8552, Japan (e-mail: amemiya@ee.e.titech.ac.jp; nishiyama@ee.e.titech.ac.jp).

Color versions of one or more figures in this article are available at https://doi.org/10.1109/JQE.2022.3145870.

Digital Object Identifier 10.1109/JQE.2022.3145870

0018-9197 © 2022 IEEE. Personal use is permitted, but republication/redistribution requires IEEE permission.
See https://www.ieee.org/publications/rights/index.html for more information.

Authorized licensed use limited to: Tokyo Institute of Technology. Downloaded on April 25,2022 at 12:14:22 UTC from IEEE Xplore. Restrictions apply.

wavelength detuning was used to compensate for the gain at high temperatures, which resulted in a 90 °C operation of the membrane DR laser [19]. However, a high thermal resistance of over 5000 K/W was experimentally estimated using a 30-μm-length DFB cavity. This was attributed to the extremely low thermal conductivity (0.29 W/ K·m) of the BCB bonding layer compared with the other materials in the laser structure, which limits the heat dissipation. Therefore, a BCB-free structure of the membrane laser and the corresponding fabrication process need to be investigated for low-thermal-resistance membrane lasers operating at high temperatures.

To achieve a BCB-free structure in a membrane laser, it is necessary to develop an appropriate direct wafer-bonding technology. Recently, various direct wafer-bonding technologies have been studied for hybrid integration [20], [21], such as hydrophilic bonding [21] and surface-activated bonding (SAB) [22], [23] based on fast atom beam (FAB) at room temperature. The laser fabricated through plasma-activated bonding with low post-annealing (<200 °C) [24]–[26] was demonstrated to reduce the influence of thermal expansion stress due to the thermal expansion coefficient difference between Si (2.6×10^{-6} /K) and InP (4.8×10^{-6} /K). Ultimately, room-temperature bonding is the most attractive method for high-quality III-V/Si hybrid integration. The SAB based on Ar-FAB has been widely studied using various semiconductor materials (sapphire, Si, GaAs, InP, and GaP) [27]. We have also demonstrated an InP-based layer/SOI Fabry-Perot (FP) laser through SAB based on Xe-FAB [28]. However, the study showed that SiO_2 was difficult to bond by SAB in both Si-to-oxide and oxide-to-oxide bonding [29]. To overcome this problem, a specific SAB using a-Si nanofilm has been demonstrated [30], [31]. In our previous report [32], a high-quality SAB of a GaInAsP/InP/SiO_2 structure bonded on Si with a-Si intermediate assisted layer was demonstrated.

In this study, we fabricated a membrane FP laser through Ar-FAB based SAB with a-Si nanofilm assisted layer for the first time and measured its thermal properties. A higher saturation current was obtained compared with the 2-μm-thick BCB-bonded membrane FP laser. The thermal resistance was estimated to be 50% lower than that of the BCB-bonded device.

Section II shows the theoretical calculation of thermal resistance using FP membrane laser model. Section III shows the design and details of fabrication process. The characteristics of fabricated devices will be discussed in section IV. Finally, the section V summarizes the whole work in this paper.

II. Analysis of Thermal Resistance

In this section, the thermal resistance is theoretically estimated. Figure 1 (a) shows the cross-sectional thermal model of the membrane laser. In the active region, Joule heat, non-radiative recombination, and optical absorption are considered as the heat powers. In the InP layers, the current path in p-InP was assumed to be the heat source owing to the Joule heat, while the resistance of the n-InP layer was negligible because the mobility of electrons in conduction band is larger than that of the holes in valence band, resulting the resistivity of p-InP is much larger than that of n-InP [33], thereby the resistance of p-InP dominated the entire resistance of membrane laser. Therefore, the heat dissipated power P_{heat} can be expressed as

$$P_{heat} = \left[IV_d - 2E_g\eta_d\,(I - I_{th})\right] + I^2(R_{act} + R_{p-InP}) \quad (1)$$

where I, V_d, and E_g are the bias current, voltage drop through the active region, and bandgap of 0.8 eV, respectively.

Figures 1 (b) and (c) show the cross-sectional temperature distribution based on the 2-μm-thick BCB and BCB-free structure of the membrane laser using the 2D finite element method. In this model, Cu heat sink was set under the membrane laser with an air gap layer of 2-μm representing the roughness between silicon substrate and Cu heat sink. In horizontal direction, the distance between n-InP and the active region was 3 μm, and that between p-InP and the active region was 1.5 μm. The average thermal conductivity was used in a bulk structure of active region as a replacement of quantum wells, barriers, and optical confinement layers. The thermal conductivities used in the simulation [34], [35] are listed in Table I. Typical steady-state heat transfer equations were used in the simulation [36]:

$$-\nabla\cdot(\kappa\nabla T) = Q \quad (2)$$

where κ is the thermal conductivity, T is the temperature, and Q is the heat density. Two boundary conditions were set for the simulations. One is the convection flux, and the other is the temperature of the heat sink, which is given by

$$\kappa\nabla T = h(T_{\text{ext}} - T) \quad (3)$$

$$T|_{heat\ sink} = T_s = 293.15\ \text{K} \quad (4)$$

where h is the heat transfer coefficient and T_s is the bottom temperature of the heat sink. The heat flux of the laser, surrounded by air in an indoor environment, was assumed to be 4.6 W/(K·m^2). The external temperature T_{ext} was set to be 293.15 K.

The initial temperature of all the solid heat-transfer modules was also set to 293.15 K. The heat dissipated power of the laser was set as 17.7 mW, with a bias current of 20 mA and differential resistance of 50 Ω. From Figs. 1(b) and (c), it can be seen that the temperature change in the active region were 4.7 and 2.3 K, respectively, which indicates that the BCB-free structure has a 50% higher heat dissipation effect compared with the 2-μm-thick BCB structure. The thermal resistance R_{th} was calculated using the following equation:

$$R_{th} = \frac{\Delta T}{P_{heat}}\ [\text{K/W}] \quad (5)$$

where ΔT is the temperature rise of the active region.

Figure 2 shows the calculated BCB thickness dependence of the thermal resistance using a 550-μm cavity length membrane FP laser model. It can be seen that there is approximately 50% thermal resistance reduction by shortening the thickness of BCB from 2 μm to 0 μm, which indicates that introducing a BCB-free structure in the membrane laser is an effective method for heat diffusion.

Authorized licensed use limited to: Tokyo Institute of Technology. Downloaded on April 25,2022 at 12:14:22 UTC from IEEE Xplore. Restrictions apply.

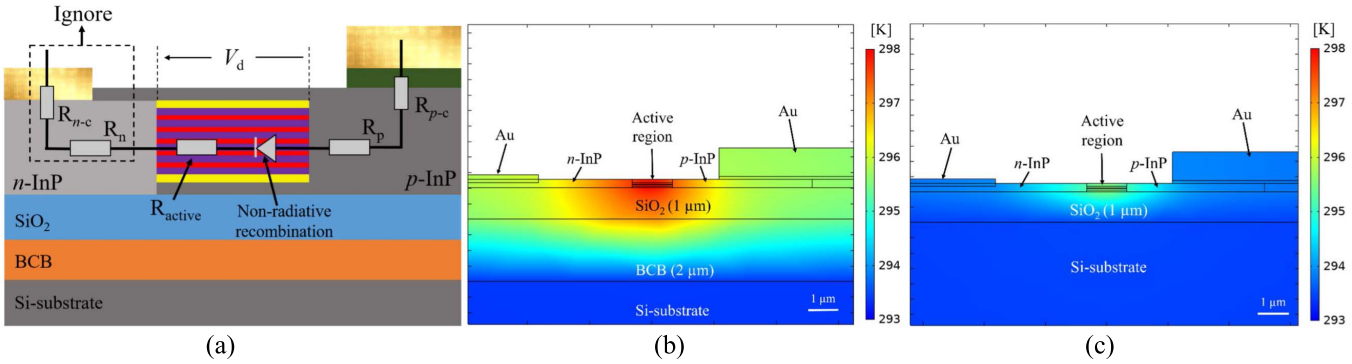

Fig. 1. (a) Thermal model of membrane laser. (b) Calculated temperature distribution based on 2D-FEM in 2-μm BCB bonding structure and in (c) BCB-free structure.

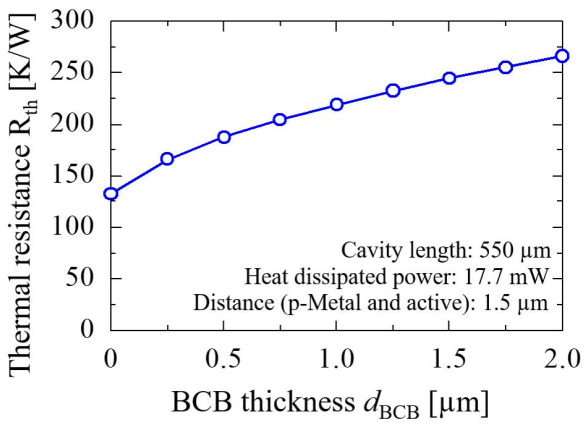

Fig. 2. Dependence of thermal resistance on BCB thickness.

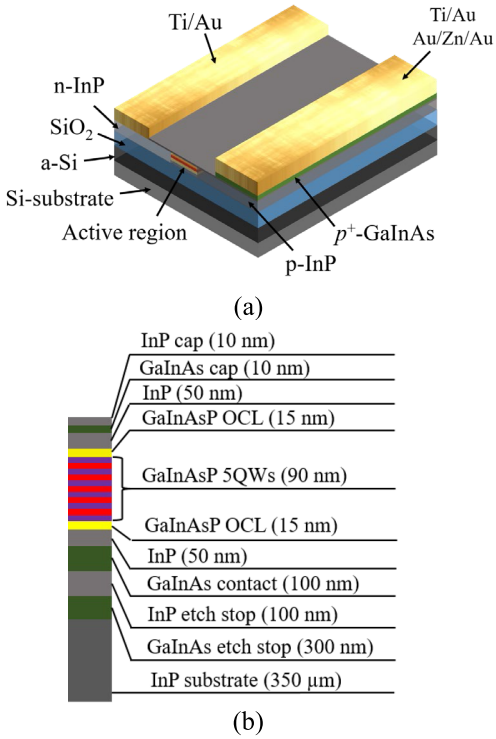

Fig. 3. (a) Schematic of direct bonded membrane FP laser using surface activated bonding. (b) Initial wafer structure.

III. Investigation of Fabeication Process

Figure 3(a) shows a schematic of the lateral-current-injection (LCI) membrane FP laser bonded by SAB. The initial wafer (Fig. 3(b)) grown on a 350-μm-thick InP substrate via organometallic vapor phase epitaxy (OMVPE) consists of a 220-nm-thick core layer comprising five GaInAsP quantum wells sandwiched by InP, p^+-GaInAs contact layer, etch stop layers, and cap layers. The core layer contains five 1% compressively strained GaInAsP wells, 0.15% tensile-strained GaInAsP barriers, undoped GaInAsP optical confinement layers (OCLs), and undoped InP layers.

The fabrication processes of BCB-bonded and BCB-free membrane FP lasers are shown in Figs. 4(a) and (b), respectively. First, after preparing the initial wafer, the n-side and p-side InP layers were formed by two-step OMVPE selective regrowth. Then, for the BCB-bonded device shown in Fig. 4(a), plasma-enhanced chemical vapor deposition (PEVCD) was used to deposit a 1-μm-thick SiO_2 layer followed by a BCB bonding process. A 2-μm-thick BCB layer was spin-coated on the Si substrate, then the Si wafer was pre-cured for 40 min in an oven where full of nitrogen at 210 °C. After that, the laser wafer was bonded on Si at 130 °C under a 25 kPa load pressure. Subsequently, for BCB solidification, the pre-bonded wafer was hard-cured in a nitrogen atmosphere oven at 250 °C for 60 min. After removing unnecessary layers, the contact layer was patterned through photolithography and wet etching, and finally, the electrodes were evaporated.

The BCB bonding process is not sensitive to the surface profiles of the wafer. However, the case of direct bonding is different. The surface profile after n-and p-side InP formation via OMVPE is shown in Fig. 5, measured using a probe-scan surface profiler. It showed an approximately 130-nm step including over-regrowth and low thickness of p-InP due to wide SiO_2 masks from the OMVPE process. Therefore, in the BCB-free process, a chemical mechanical polishing (CMP) process should be introduced to flatten the SiO_2 surface. The change process is illustrated in Fig. 4(b). The 2-μm-thick SiO_2 was deposited, then about 1-μm-thick SiO_2 was removed for

Authorized licensed use limited to: Tokyo Institute of Technology. Downloaded on April 25,2022 at 12:14:22 UTC from IEEE Xplore. Restrictions apply.

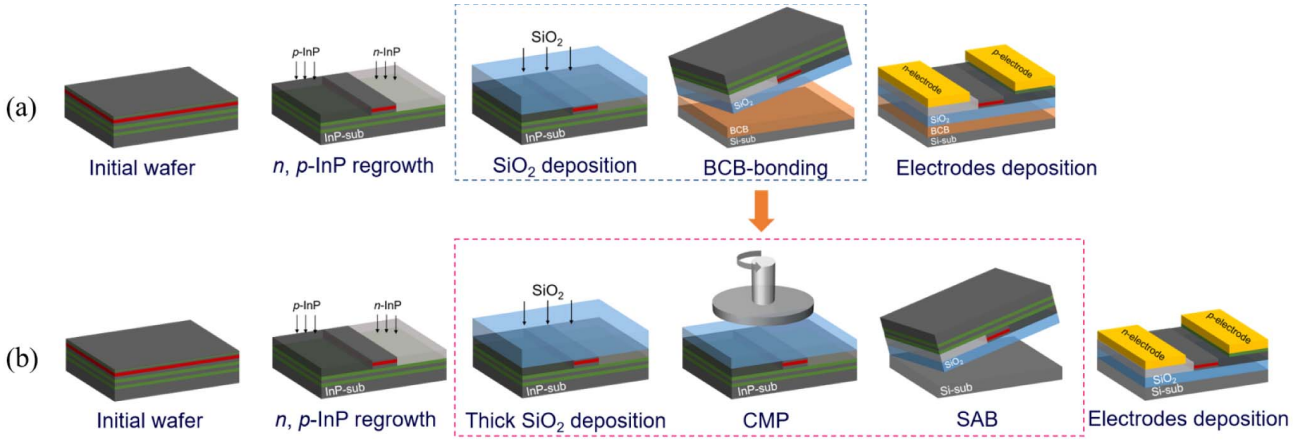

Fig. 4. Membrane FP laser fabrication process of (a) BCB bonding structure and (b) BCB-free structure.

TABLE I
THERMAL CONDUCTIVITY USED IN SIMULATION [34], [35]

Material	Thermal conductivity [W/(K·m)]
Cu	400
Au	320
InP	68
Si	158
GaInAsP (active)	5
GaInAs (contact layer)	4.4
SiO_2	1.4
BCB	0.29

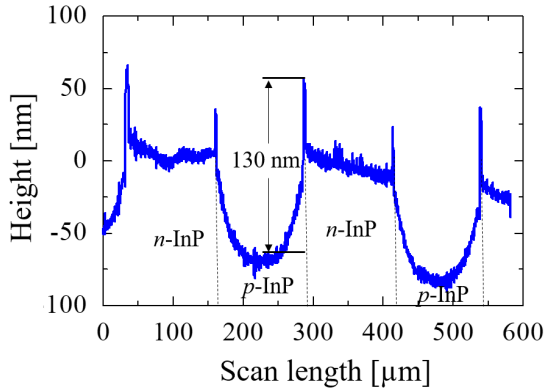

Fig. 5. Surface shape before bonding process.

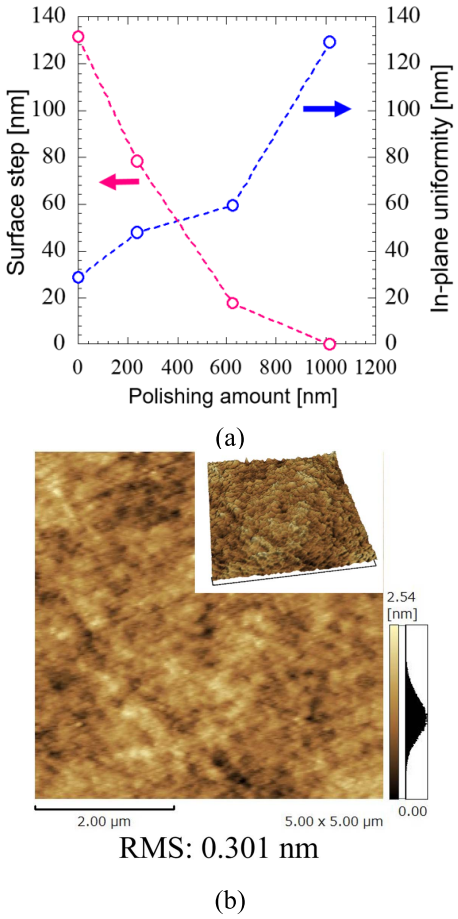

Fig. 6. (a) Surface step and in-plane uniformity dependence on polishing amount. (b) Surface roughness after polishing 1-μm-SiO_2 using slurry of Semi-sperse 25.

CMP planarization. As the result, the remained thickness of SiO_2 was 1 μm. Then, CMP and SAB assisted by an a-Si nanofilm at room temperature were carried out.

For the CMP process, the slurry used for SiO_2 polishing in the experiment was Semi-sperse 25. The process was performed under in-situ polishing conditions (while polishing the wafer, the polishing pad was polished using a pad conditioner simultaneously) with a polishing-pad/wafer rotation speed of 40/41 rpm, pressure of 50 g/cm^2, and slurry flow rate of 100 ml/min. Figure 6(a) shows the macroscopic results of polishing with an initial surface step of 130 nm in the same condition after two-step OMVPE regrowth. The results showed that a polishing amount of at least 1000 nm was needed to obtain a relatively flat surface. However, at the same time,

Authorized licensed use limited to: Tokyo Institute of Technology. Downloaded on April 25,2022 at 12:14:22 UTC from IEEE Xplore. Restrictions apply.

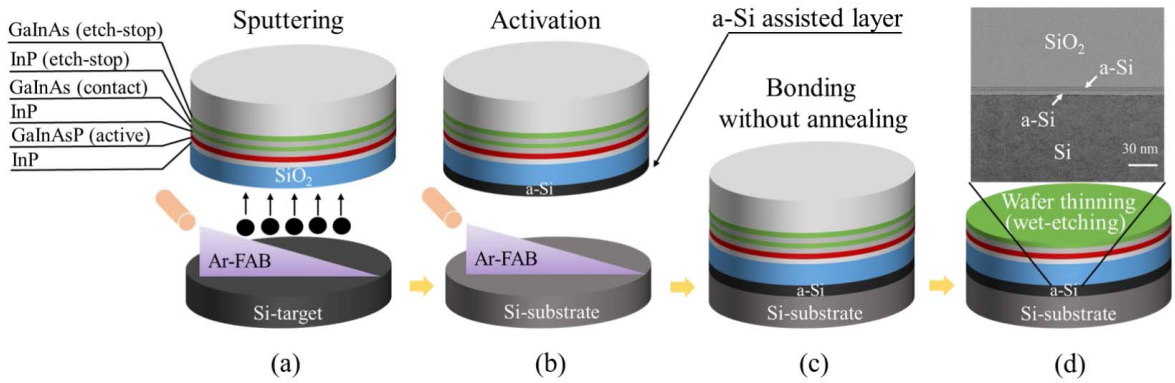

Fig. 7. Surface activated bonding process assisted by a-Si nano-film. (a) Ar-FAB irradiation for a-Si sputtering. (b) Si-substrate surface activation using Ar-FAB. (c) Room temperature bonding. (d) Removing unnecessary layers by selective wet-etching and TEM image of bonding interface.

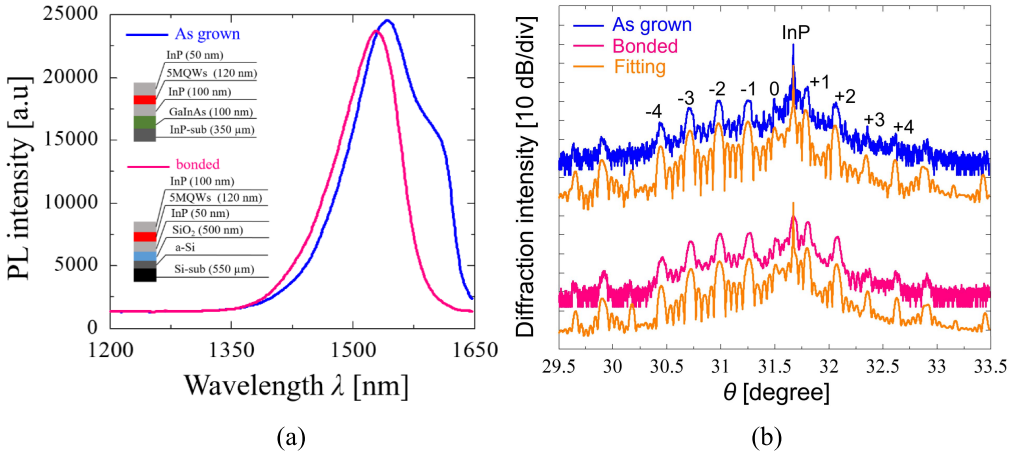

Fig. 8. (a) PL intensity before and after bonding using a test wafer. (b) Measured and fitting calculated XRD data of as-grown and bonded wafer.

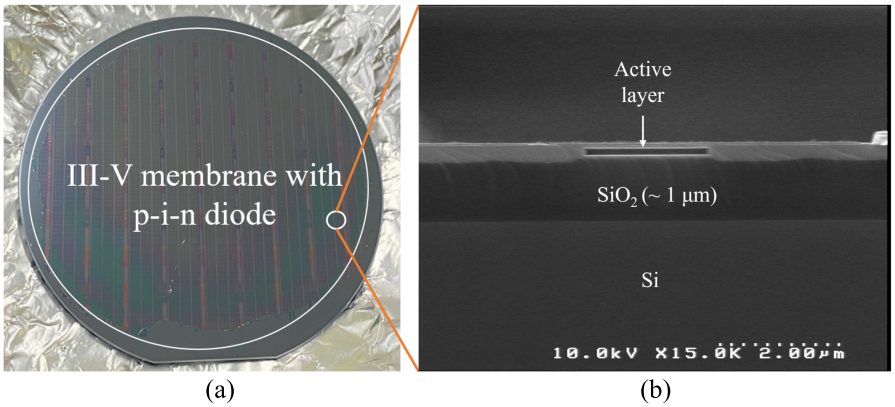

Fig. 9. Images of fabricated device. (a) Bonding area after CMP-SAB with p-i-n diode structure. (b) SEM image of fabricated device by SAB.

there was a difference of over 100 nm between the edge and center of the wafer after 1000 nm polishing. The value of in-plane uniformity (difference in peak-to-peak SiO_2 thickness), estimated through 17 points of SiO_2 thickness distributed in a 2-inch wafer, increased monotonically as the polishing amount increased. Therefore, an approximately 1000 nm polishing amount can be used in the fabrication process. Figure 6(b) shows the surface roughness after polishing with 1000 nm SiO_2, measured using atomic force microscopy (AFM). The root mean square (RMS) value was 0.301 nm, which meets the ideal value of less than 0.5 nm for direct bonding [37].

Figure 7 shows the details of the surface-activated bonding process assisted by the Si nanofilm. All the processes were performed under a high-vacuum atmosphere ($<10^{-5}$ Pa). First, the laser wafer and target Si wafer as the sputtering source were chucked at the upper and bottom sides of the

Authorized licensed use limited to: Tokyo Institute of Technology. Downloaded on April 25,2022 at 12:14:22 UTC from IEEE Xplore. Restrictions apply.

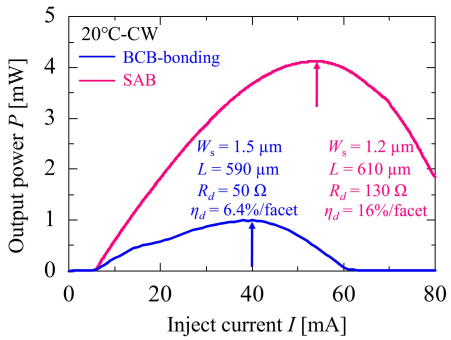

Fig. 10. I–L characteristics of devices fabricated via SAB and BCB-bonding.

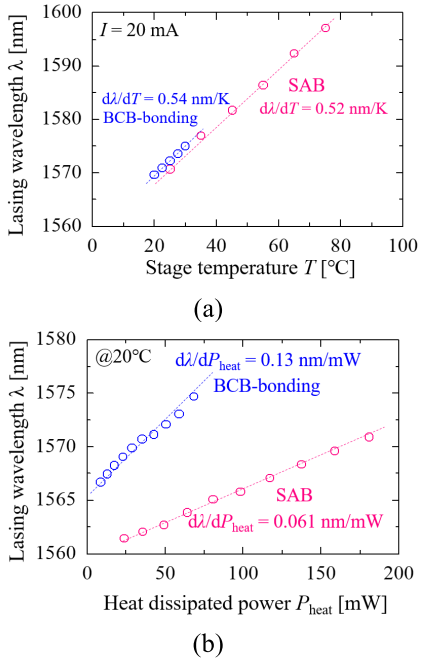

Fig. 11. (a) Temperature dependence of the lasing wavelength measured at a fixed injection current of 20 mA. (b) Lasing wavelength of BCB-bonded and SAB devices as a function of heat dissipated power measured at 20°C.

chamber, respectively. Then, Ar-FAB was used to irradiate the target Si wafer under an Ar flow of 30 sccm, a current of 100 mA, a voltage of 1.5 kV, and an irradiation time of 15 min. Using this irradiation, the surface of SiO_2 was formed a sputtered a-Si nanofilm (Fig. 7(a)). Subsequently, a new Si wafer was introduced into chamber for replacing the target Si sputtering source. Then, Ar-FAB was used to activate the new Si wafer under an Ar flow of 30 sccm, a current of 50 mA, a voltage of 1.2 kV, and an irradiation time of 90 s (Fig. 7(b)). Finally, two wafers were bonded without any heat for 5 min under a pressure of 500 kgf (Fig. 7(c)). After bonding, selective wet etching was performed to remove unnecessary layers (Fig. 7(d)). The transmission electron microscope (TEM) image shows detailed information about the a-Si bonding layer. Two a-Si layers were observed at the bonding interface. The upper layer was the sputtered a-Si layer, and the bottom layer was formed by Ar-FAB irradiation in the activation step of the bonding process.

Figure 8(a) shows the photoluminescence (PL) intensity before and after bonding using a test wafer. The shoulder around 1630 nm indicates the peak of the GaInAs

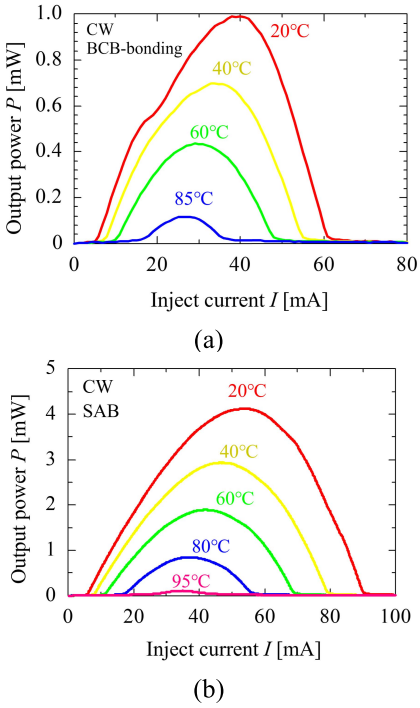

Fig. 12. I-L characteristics under various stage temperature of devices fabricated via (a) BCB-bonding and (b) SAB.

etch-stop layer in the as-grown wafer, and the etch-stop layer was removed in bonded wafer. No obvious degradation was observed after bonding, and the small peak wavelength blueshift was due to the compressive strain relaxation when removed 350-μm-thick InP-substrate. Figure 8(b) shows the measured and the calculated XRD ω-2θ scan data. The InP peak was reduced in the bonded wafer because the thick InP substrate was removed by wet etching, and the peak was dominated by InP (150 nm in total) inside the core layer. Based on the measurement, the relative positions of satellite peaks from "−4" to "4" were well-maintained after bonding. The fitting calculation reveals that the net strain in the multi-quantum-wells reduced from 0.50% to 0.47%, which manifested a peak wavelength blueshift in the PL measurement.

Figure 9(a) shows the bonding area during the fabrication of the membrane laser with a p-i-n diode structure. A large enough area of bonding was obtained, and the scanning electron microscope (SEM) image of the device is shown in Fig. 9(b). A flat bonding interface between the Si and SiO_2 layers was achieved owing to the CMP planarization. It seems that the 100 nm SiO_2 film thickness that slowly changes within the 2-inch wafer size range did not have a major impact on the direct bonding process. Based on the discussion above, a BCB-free process for the membrane laser was successfully developed.

IV. Device Characteristics

Figure 10 shows the light output characteristics of BCB-bonded and BCB-free (using SAB) membrane FP lasers in room temperature continuous wave conditions (RT-CW). The stripe width, cavity length, differential resistance, and external differential quantum efficiency were $W_s = 1.5$ μm,

Authorized licensed use limited to: Tokyo Institute of Technology. Downloaded on April 25,2022 at 12:14:22 UTC from IEEE Xplore. Restrictions apply.

$L = 590\ \mu$m, $R_d = 50\ \Omega$, and $\eta_d = 6.4\%$/facet, respectively, in the BCB- bonded device and $W_s = 1.2\ \mu$m, $L = 610\ \mu$m, $R_d = 130\ \Omega$, and $\eta_d = 16\%$/facet, respectively in the SAB device. The threshold current of both devices was around 5.5 mA. A higher differential resistance in SAB device was due to a larger distance between p-electrode and active layer. Even with this problem, a higher output power and optical saturation current were obtained for the SAB device, indicating a structure with higher heat dissipation.

Figure 11(a) shows the temperature dependence of the lasing wavelength under a fixed injection current of 20 mA. The slopes of 0.54 nm/K and 0.52 nm/K were obtained for the BCB-bonded and SAB devices, respectively. This difference contributed to the measurement error. The thicknesses of the Si substrates in the BCB-bonded and SAB devices were 150 μm and 550 μm, respectively, which caused a slightly different temperature distribution in the active region when the stage temperature changed. Figure 11(b) shows the lasing wavelength as a function of heat dissipated power (a product of the injected current and the bias voltage minus the output power) at a fixed temperature of 20 °C. The average slopes for the BCB-bonded and SAB devices were 0.13 nm/mW and 0.061 nm/mW, respectively, and the thermal resistances were calculated to be approximately 240 K/W and 120 K/W, respectively. The thermal resistance was reduced by approximately 50%, according to the experimental results, which agreed with the simulation results.

Figure 12 shows the I-L characteristics of both BCB-bonding and SAB device under various stage temperature. Compared with BCB-bonded device, a higher lasing temperature up to 95°C was obtained in SAB membrane FP laser thanks to the lower thermal resistance.

V. Conclusion

We first theoretically analyzed the thermal resistance of a membrane FP laser. The results showed that the temperature rise of the active region in the BCB-free structure was 50% lower than that in the conventional 2-μm-thick BCB-bonded structure; moreover, a 50% reduction in thermal resistance was observed when the BCB thickness was reduced from 2 μm to 0 μm. We then constructed a BCB-free structure fabrication process for the membrane laser in order to reduce the thermal resistance. A CMP process was used to flatten the surface of the SiO_2 layer after two-step OMVPE regrowth. Surface-activated bonding using an Ar fast atom beam assisted by an a-Si nanofilm was used to bond SiO_2 and Si at room temperature. As a result, a large bonding area and low strain bonding were achieved, and no threading dislocations were observed. Using the process described above, a BCB-free membrane FP laser was fabricated. Compared with that for the conventional device with a 2-μm-thick BCB layer, a higher optical saturation current was obtained even with a higher differential resistance, and a 50% lower thermal resistance was experimentally confirmed. In the future works, a low thermal resistance membrane DFB and DR laser will be fabricated using this room temperature bonding and higher temperature and higher modulation speed operations can be expected.

References

[1] R. H. Dennard, "Past progress and future challenges in LSI Technology: From DRAM and scaling to ultra-low-power CMOS," *IEEE Solid-State Circuits Mag.*, vol. 7, no. 2, pp. 29–38, 2015.

[2] P. Kapur, J. P. McVittie, and K. C. Saraswat, "Technology and reliability constrained future copper interconnects. I. Resistance modeling," *IEEE Trans. Electron Devices*, vol. 49, no. 4, pp. 590–597, Apr. 2002.

[3] J. Jiang, Z. Mao, W. Sheng, Q. Wang, and W. He, "Delay analysis and design optimization for low-swing RC-limited global interconnects," *J. Circuits, Syst. Comput.*, vol. 25, no. 10, Oct. 2016, Art. no. 1650121.

[4] S. Jadav, M. Vashishath, and R. Chandel, "High speed RLC equivalent RC delay model for global VLSI interconnects," *Anal. Integr. Circuits Signal Process.*, vol. 100, no. 1, pp. 109–117, Jul. 2019.

[5] M. Haurylau *et al.*, "On-chip optical interconnect roadmap: Challenges and critical directions," *IEEE J. Sel. Topics Quantum Electron.*, vol. 12, no. 6, pp. 1699–1705, Nov./Dec. 2006.

[6] D. A. B. Miller, "Device requirements for optical interconnects to silicon chips," *Proc. IEEE*, vol. 97, no. 7, pp. 1166–1185, Jul. 2009.

[7] K. Ohashi *et al.*, "On-chip optical interconnect," *Proc. IEEE*, vol. 97, no. 7, pp. 1186–1198, Jul. 2009.

[8] M. Stucchi, S. Cosemans, J. Van Campenhout, Z. Tőkei, and G. Beyer, "On-chip optical interconnects versus electrical interconnects for high-performance applications," *Microelectron. Eng.*, vol. 112, pp. 84–91, Dec. 2013.

[9] N. Haghighi, P. Moser, and J. A. Lott, "Power, bandwidth, and efficiency of single VCSELs and small VCSEL arrays," *IEEE J. Sel. Topics Quantum Electron.*, vol. 25, no. 6, pp. 1–15, Nov. 2019.

[10] Z. Khan *et al.*, "High-brightness and high-speed vertical-cavity surface-emitting laser arrays," *Optica*, vol. 7, no. 4, pp. 267–275, Mar. 2020.

[11] S. Matsuo *et al.*, "High-speed ultracompact buried heterostructure photonic-crystal laser with 13 fJ of energy consumed per bit transmitted," *Nature Photon.*, vol. 4, no. 9, pp. 648–654, Sep. 2010.

[12] S. Matsuo and K. Takeda, "λ-scale embedded active region photonic crystal (LEAP) lasers for optical interconnects," *Photonics*, vol. 6, no. 3, p. 82, Jul. 2019.

[13] C.-T. Chen *et al.*, "Chip-level 1×2 optical interconnects using polymer vertical splitter on silicon substrate," *IEEE Photon. J.*, vol. 6, no. 2, pp. 1–10, Apr. 2014.

[14] K. Takeda *et al.*, "Few-fJ/bit data transmissions using directly modulated lambda-scale embedded active region photonic-crystal lasers," *Nature Photon.*, vol. 7, pp. 569–575, Jul. 2013.

[15] T. Okamoto, N. Nunoya, Y. Onodera, S. Tamura, and S. Arai, "Continuous wave operation of optically pumped membrane DFB laser," *Electron. Lett.*, vol. 37, no. 24, pp. 1455–1457, Nov. 2001.

[16] T. Hiratani *et al.*, "Room-temperature continuous-wave operation of membrane distributed-reflector laser," *Appl. Phys. Exp.*, vol. 8, no. 11, Oct. 2015, Art. no. 112701.

[17] T. Tomiyasu *et al.*, "High-differential quantum efficiency operation of GaInAsP/InP membrane distributed-reflector laser on Si," *Appl. Phys. Exp.*, vol. 10, no. 6, May 2017, Art. no. 062702.

[18] T. Tomiyasu *et al.*, "20-Gbit/s direct modulation of GaInAsP/InP membrane distributed-reflector laser with energy cost of less than 100 fJ/bit," *Appl. Phys. Exp.*, vol. 11, no. 1, Dec. 2017, Art. no. 012704.

[19] T. Hiratani *et al.*, "90 °C continuous-wave operation of GaInAsP/InP membrane distributed-reflector laser on Si substrate," *Appl. Phys. Exp.*, vol. 10, no. 3, Feb. 2017, Art. no. 032702.

[20] S. Bao *et al.*, "A review of silicon-based wafer bonding processes, an approach to realize the monolithic integration of Si-CMOS and III–V-on-Si wafers," *J. Semicond.*, vol. 42, no. 2, Feb. 2021, Art. no. 023106.

[21] V. Masteika, J. Kowal, N. S. J. Braithwaite, and T. Rogers, "A review of hydrophilic silicon wafer bonding," *ECS J. Solid State Sci. Technol.*, vol. 3, no. 4, pp. Q42–Q54, Feb. 2014.

[22] H. Takagi, K. Kikuchi, R. Maeda, T. R. Chung, and T. Suga, "Surface activated bonding of silicon wafers at room temperature," *Appl. Phys. Lett.*, vol. 68, no. 16, pp. 2222–2224, Apr. 1996.

[23] H. Takagi, R. Maeda, N. Hosoda, and T. Suga, "Transmission electron microscope observations of Si/Si interface bonded at room temperature by Ar beam surface activation," *Jpn. J. Appl. Phys.*, vol. 38, pp. 1589–1594, Mar. 1999.

[24] Y. Hayashi *et al.*, "Low threshold current density operation of a GaInAsP/Si hybrid laser prepared by low-temperature N_2 plasma activated bonding," *Jpn. J. Appl. Phys.*, vol. 52, no. 6R, Jun. 2013, Art. no. 060202.

Authorized licensed use limited to: Tokyo Institute of Technology. Downloaded on April 25,2022 at 12:14:22 UTC from IEEE Xplore. Restrictions apply.

[25] S. Matsuo, T. Fujii, K. Hasebe, K. Takeda, T. Sato, and T. Kakitsuka, "Directly modulated buried heterostructure DFB laser on SiO_2/Si substrate fabricated by regrowth of InP using bonded active layer," *Opt. Exp.*, vol. 22, no. 10, pp. 12139–12147, May 2014.
[26] T. Fujii *et al.*, "Multiwavelength membrane laser array using selective area growth on directly bonded InP on SiO_2/Si," *Optica*, vol. 7, pp. 838–846, Jul. 2020.
[27] T. R. Chung, L. Yang, N. Hosoda, H. Takagi, and T. Suga, "Wafer direct bonding of compound semiconductors and silicon at room temperature by the surface activated bonding method," *Appl. Surf. Sci.*, vol. 117, pp. 808–812, Jun. 1997.
[28] Y. Wang, K. Nagasaka, T. Mitarai, Y. Ohiso, T. Amemiya, and N. Nishiyama, "High-quality InP/SOI heterogeneous material integration by room temperature surface-activated bonding for hybrid photonic devices," *Jpn. J. Appl. Phys.*, vol. 59, no. 5, Apr. 2020, Art. no. 052004.
[29] H. Takagi, J. Utsumi, M. Takahashi, and R. Maeda, "Room-temperature bonding of oxide wafers by Ar-beam surface activation," *ECS Trans.*, vol. 16, no. 8, pp. 531–537, Dec. 2019.
[30] J. Utsumi, K. Ide, and Y. Ichiyanagi, "Room temperature bonding of SiO_2 and SiO_2 by surface activated bonding method using Si ultrathin films," *Jpn. J. Appl. Phys.*, vol. 55, no. 2, Jan. 2016, Art. no. 026503.
[31] R. Takigawa and T. Asano, "Thin-film lithium niobate-on-insulator waveguides fabricated on silicon wafer by room-temperature bonding method with silicon nanoadhesive layer," *Opt. Exp.*, vol. 26, no. 19, pp. 24413–24421, Sep. 2018.
[32] W. Fang, N. Takahashi, Y. Ohiso, T. Amemiya, and N. Nishiyama, "High-quality, room-temperature, surface-activated bonding of GaInAsP/InP membrane structure on silicon," *Jpn. J. Appl. Phys.*, vol. 59, no. 6, Jun. 2020, Art. no. 060905.
[33] T. Hiratani *et al.*, "Energy cost analysis of membrane distributed-reflector lasers for on-chip optical interconnects," *IEEE J. Sel. Topics Quantum Electron.*, vol. 21, no. 6, pp. 299–308, Nov. 2015.
[34] W. Nakwaski, "Thermal conductivity of binary, ternary, and quaternary III–V compounds," *J. Appl. Phys.*, vol. 64, no. 1, pp. 159–166, Jul. 1988.
[35] K. Doi, T. Shindo, J. Lee, T. Amemiya, N. Nishiyama, and S. Arai, "Thermal analysis of lateral-current-injection membrane distributed feedback laser," *IEEE J. Quantum Electron.*, vol. 50, no. 5, pp. 321–326, May 2014.
[36] H. K. Lee, Y. M. Song, Y. T. Lee, and J. S. Yu, "Thermal analysis of asymmetric intracavity-contacted oxide-aperture VCSELs for efficient heat dissipation," *Solid-State Electron.*, vol. 53, no. 10, pp. 1086–1091, Oct. 2009.
[37] V. Dragoi, B. Rebhan, and E. Pabo, "Direct wafer bonding methods: A practical process selection guide," *ECS Trans.*, vol. 98, no. 4, pp. 33–46, Sep. 2020.

Weicheng Fang was born in Wuhan, China, in 1994. He received the B.E. degree in information science and technology from the Wenhua College, Huazhong University of Science and Technology, Wuhan, in 2017, and the M.E. degree in electrical and electronic engineering from the Tokyo Institute of Technology, Tokyo, Japan, in 2019, where he is currently pursuing the Ph.D. degree in electrical and electronic engineering.

His current research interests include membrane-based photonic devices for optical interconnection.

Mr. Fang is a Student Member of the Institute of Electronics, Information and Communication Engineers, and the Japan Society of Applied Physics.

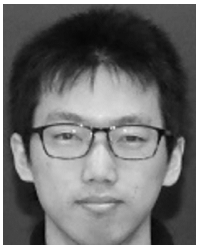

Naoki Takahashi was born in Chiba, Japan, in 1997. He received the B.E. and M.E. degrees in electrical and electronic engineering from the Tokyo Institute of Technology, Tokyo, Japan, in 2019 and 2021, respectively, where he is currently pursuing the Ph.D. degree in electrical and electronic engineering.

His current research interest includes membrane-based photonic devices for optical interconnection.

Mr. Takahashi is a Student Member of the Institute of Electronics, Information and Communication Engineers, and the Japan Society of Applied Physics.

Yoshitaka Ohiso was born in Tokyo, Japan, in 1965. He received the B.S., M.S., and Ph.D. degrees in electrical engineering from Keio University, Yokohama, Japan, in 1989, 1991, and 2003, respectively.

Since joining NTT Laboratories, Kanagawa, Japan, in 1991, he has been engaged in the research and development of optical semiconductor devices, such as VCSEL, optical filters, and the optical modulator of EA and MZM. He has also been engaged in the epitaxial growth of III–V compound semiconductors by MOCVD. He is currently a Specially Appointed Associate Professor with the Tokyo Institute of Technology, Tokyo.

Dr. Ohiso is a member of the Japan Society of Applied Physics and the Institute of Electronics Information and Communication Engineers of Japan.

Tomohiro Amemiya (Member, IEEE) was born in Tokyo, Japan, in 1981. He received the B.S., M.S., and Ph.D. degrees in electronic engineering from The University of Tokyo, Japan, in 2004, 2006, and 2009, respectively.

In 2009, he moved to the Quantum Electronics Research Center (QNERC), Tokyo Institute of Technology, where he is currently an Assistant Professor. His research interests are in the physics of semiconductor light-controlling devices, metamaterials for optical frequencies, magneto-optical devices, and the technologies for fabricating these devices.

Dr. Amemiya was a recipient of the 2007 IEEE Photonics Society Annual Student Paper Award, the 2008 IEEE Photonics Society Graduate Student Fellowships, the 2012 Konica Minolta Imaging Award, the 2015 Yazaki Memorial Foundation Award, the 2016 Young Scientists' Prize, and the Commendation for Science and Technology by the Minister of Education, Culture, Sports, Science and Technology (MEXT).

Nobuhiko Nishiyama (Senior Member, IEEE) was born in Yamaguchi, Japan, in 1974. He received the B.E., M.E., and Ph.D. degrees from the Tokyo Institute of Technology, Japan, in 1997, 1999, and 2001, respectively.

During his Ph.D. work, he demonstrated single-mode 0.98 and 1.1-μm VCSEL arrays with stable polarization using misoriented substrates for high-speed optical networks and MOCVD-grown GaInNAs VCSELs. He joined Corning, Inc., New York, in 2001, and worked with the Semiconductor Technology Research Group. At Corning, he worked on several subjects, including short-wavelength lasers, 1060-nm DFB/DBR lasers, and long wavelength InP-based VCSELs. He has been an Associate Professor since 2006 and a Professor since 2020 with the Tokyo Institute of Technology. His current research interests include III–V silicon hybrid photonic integrated circuit, silicon photonics, transistor lasers, and terahertz–optical signal conversions involving optics–electronics–radio integration circuits.

Dr. Nishiyama is a member of the Japan Society of Applied Physics (JSAP) and IEICE. During 2018–2020, he was appointed as the Board of Governor of the IEEE Photonic Society. He was a recipient of the Excellent Paper Award from the Institute of Electronics, Information and Communication Engineers (IEICE) of Japan in 2001, the Young Scientists' Prize of the Commendation for Science and Technology from the Minister of Education, Culture, Sports, Science and Technology in 2009, and the Ichimura Prize in Science for Distinguished Achievement in 2016.

Authorized licensed use limited to: Tokyo Institute of Technology. Downloaded on April 25,2022 at 12:14:22 UTC from IEEE Xplore. Restrictions apply.